

Impact of the collective diffusion of charged nanoparticles in the convective/capillary deposition directed by receding contact lines^{*,**}

Diego Noguera-Marín¹, Carmen Lucía Moraila-Martínez², Miguel Cabrerizo-Vílchez¹, and Miguel Ángel Rodríguez-Valverde^{1,a}

¹ Biocolloid and Fluid Physics Group, Applied Physics Department, Faculty of Sciences, University of Granada, E-18071 Granada, Spain

² University of Sinaloa, Mexico

Received 16 June 2015 and Received in final form 26 October 2015

Published online: 26 February 2016 – © EDP Sciences / Società Italiana di Fisica / Springer-Verlag 2016

Abstract. The motion of electrically charged particles under crowding conditions and subjected to evaporation-driven capillary flow might be ruled by collective diffusion. The concentration gradient developed inside an evaporating drop of colloidal suspension may reduce by diffusion the number of particles transported toward the contact line by convection. Unlike self-diffusion coefficient, the cooperative diffusion coefficient of interacting particles becomes more pronounced in crowded environments. In this work, we examined experimentally the role of the collective diffusion of charge-stabilized nanoparticles in colloidal patterning. To decouple the sustained evaporation from the contact line motion, we conducted evaporating menisci experiments with driven receding contact lines at low capillary number. This allowed us to explore convective assembly at fixed and low bulk concentration, which enabled to develop high concentration gradients. At fixed velocity of receding contact line, we explored a variety of substrate-particle systems where the particle-particle electrostatic interaction was changed (via *pH*) as well as the substrate receding contact angle and the relative humidity. We found that the particle deposition directed by receding contact lines may be controlled by the interplay between evaporative convection and collective diffusion, particularly at low particle concentration.

1 Introduction

Colloidal assembly by convective/capillary deposition is used for particle templating in emerging areas such as nanostructure engineering, electro-optics, chemical and biological sensors, catalysis and membranes [1]. It is well-established that inside evaporating sessile drops with contact angles lower than 90° and pinned triple contact lines, a convective flow is produced due to the significant loss of liquid in the vicinity of the contact line where the evaporation rate is divergent [2]. The velocity field in the drop is space- and time-dependent and it further depends on the substrate contact angle. Small contact angles increase the diverging evaporation rate along the contact line [2, 3]. When the evaporating drop contains colloidal particles, this evaporation-driven capillary flow transports the

particles towards the contact line from the drop bulk and a particle concentration gradient should exist in the drop. Deegan *et al.* [4] neglected the diffusion of solute in their theory but they noticed that “if the size of the solute particles is small, diffusive currents become comparable to the advective current”.

Since the local gradient of particle concentration increases for evaporation, the Fick’s law establishes that an inward flow is created by particle cooperative diffusion. This flow intends to balance the solute concentration in bulk. This way, at least two opposing flows may occur in a pinned evaporating drop of colloidal particles (see fig. 1). In absence of other significant flows of different origin, the competition between both convective and diffusive flows might dictate the final deposit shape [5,6] or even the suppression of deposit [7,6], if the particles mostly diffuse away from the contact line.

In dense systems, mutual or collective diffusion takes relevance rather than self-diffusion (individual motion of one particle in a suspension induced by impacts of solvent molecules). At high particle concentrations, many-body direct and hydrodynamic interactions must be considered to correctly describe the collective diffusion behavior [8].

* Contribution to the Topical Issue “Wetting and Drying: Physics and Pattern Formation”, edited by Duyang Zang, Ludovic Pauchard and Wei Shen.

** Supplementary material in the form of four pdf files available from the Journal web page at

<http://dx.doi.org/10.1140/epje/i2016-16020-y>

^a e-mail: marodri@ugr.es

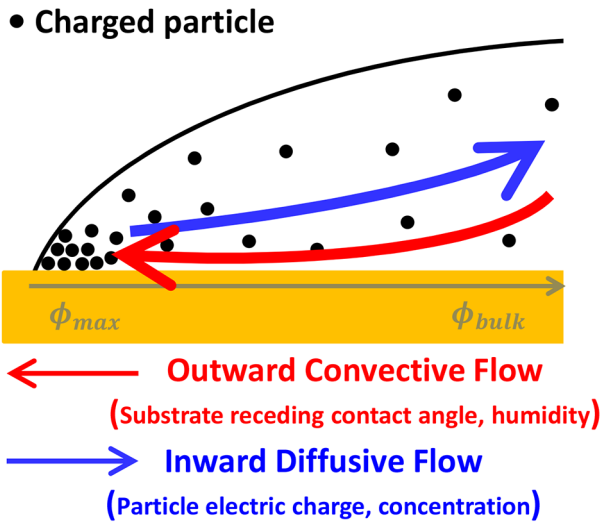


Fig. 1. Flows developed near the receding contact line of evaporating sessile drops containing charged nanoparticles: outward evaporation-driven flow and inward concentration gradient-driven flow.

In hard-sphere suspensions, the hydrodynamic interaction between the particles slows down their diffusional motion and almost cancels the increase of osmotic compressibility. Otherwise, in highly charged suspensions at low concentrations, the hydrodynamic interaction may even enhance diffusion [8]. Further, the interparticle repulsion leads to an enhancement of collective diffusion [9–11]. Close to the random-close-packing fraction, although the assembly of interacting particles still presents a finite permeability, the osmotic compressibility diverges as the direct interparticle interactions. Due to this, the collective diffusion coefficient rapidly diverges around the maximum packing fraction [12, 13].

Interparticle and substrate-particle electrostatic interactions may alter the particle deposition/patterning [14–19]. Recently, several experimental works have stressed the role of the electric charge of colloidal particles in the solidification of suspensions with an enhanced collective diffusion [20–22]. The transition between structures of charged silica nanoparticles formed by varying the environmental pressure of evaporating drops, as reported by Askounis *et al.* [23], might also reveal the competition between both convective and diffusive flows. However, in freely evaporating drop experiments, the particle concentration in bulk increases as the drop volume decreases [24]. This can significantly reduce the concentration gradient at the triple line and in consequence, no effect on the particle deposits is observed due to the collective diffusion. Besides, the complex diffusional properties of colloidal suspensions (space- and time-dependent field) are hardly measurable in situ for an experiment of drying drop.

In this work, we studied the effects caused by the collective diffusion of charged nanoparticles on the colloidal patterning produced by driven contact lines of receding menisci at low capillary number like in dip-coating experiments. Unlike free evaporation experiments, in our ap-

proach the particle concentration in bulk remains constant during the entire experiment and the effects due to the particle concentration gradient at the contact line can be noticeable. With fixed values of velocity of driven triple line and nanoparticle concentration, we explored a variety of substrate-particle systems where the particle-particle electrostatic interaction was changed (via *pH*) as well as the evaporative flux through the relative humidity and the receding contact angle by using two substrates: glass and PMMA. Finally, we examined the effect of nanoparticle concentration on the patterning when the electrostatic particle-particle repulsion was minimized and enhanced, separately.

2 Materials and methods

2.1 Substrates

We employed glass microscope cover slips (0.1 mm thick, $60 \times 24 \text{ mm}^2$, Menzel-Glaser) and polymethylmethacrylate (PMMA, 1.1 mm thick, CQ grade, Goodfellow) as substrates for the deposit formation. We selected these materials by their different and stable wettability response, transparency and purity degree. To obtain substrates of similar dimensions, the PMMA sheets was adequately cut into pieces of $60 \times 24 \text{ mm}^2$. Before each experiment, the PMMA surfaces were cleaned ultrasonically in a detergent solution (Micro90) for 10 min, followed by a prolonged ultrasonic rinsing in Milli-Q water (20 min). The glass surfaces were sonicated in the detergent solution (15 min), next in a solution of 70% (v/v) acetone (25 min), then in a solution of 70% (v/v) ethanol (15 min) and finally in Milli-Q water (15 min).

The roughness of the substrates was measured from their 3D topographies acquired with a white light confocal microscope (PL μ , Sensofar Tech S.L.). The values obtained for the root mean square roughness were 6.5 nm and $< 25 \text{ nm}$ for glass and PMMA, respectively. The roughness of the two substrates at maximum vertical resolution and minimum horizontal scale was lower than the sizes of the particles studied.

To characterize the substrate contact angle hysteresis, we measured the water advancing (θ_a) and receding contact angles (θ_r) with the captive bubble method [25]. We employed this method due to the low receding contact angle of the glass substrates (lower than 20°). Moreover, captive bubble experiments are closer to the experimental conditions of the driven menisci experiments: moving contact lines on a previously wetted surface. Details of the experimental set-up used for contact angle measurements is described elsewhere [25]. Drop profiles were analyzed with the Axisymmetric Drop Shape Analysis-Profile (ADSA-P) technique. With this approach, the drop parameters such as contact angle, contact radius, area, volume and surface tension were extracted. We used Milli-Q water for the captive bubble experiments. The air was injected/suctioned with a microinjector (PSD3, Hamilton) and a $250 \mu\text{l}$ syringe (Hamilton). The air volume was exchanged to the captive bubble at quadratic flow rate [26].

Initially, a $20\ \mu\text{l}$ bubble was injected to produce a centered growing bubble and the maximum bubble volume was $120\ \mu\text{l}$. As expected from previous studies on surface energy [27], the contact angle hysteresis of the glass substrates was negligible ($\theta_a = 16 \pm 4^\circ$ and $\theta_r = 10 \pm 3^\circ$) compared with the PMMA substrates ($\theta_a = 93 \pm 1^\circ$ and $\theta_r = 62 \pm 1^\circ$) [28]. The water receding contact angle of these substrates did not depend on the $p\text{H}$ value.

2.2 Nanoparticle suspensions

For the experiments of driven receding menisci, we used commercial aqueous suspensions of spherical nanoparticles. We selected particles with properties (wettability and electric charge) similar to the substrates selected. We purchased nanoparticles of glass (AttendBio Research, 50 nm), PMMA (Microparticles, 130 nm) and silica (SiO_2 , 90 nm, kindly supplied by Klebosol). The maximum particle concentration (w/w) of these suspensions was $\Phi_m = 50\%$ (for glass and SiO_2) and 5% for PMMA. The electric charge of the glass and SiO_2 particles is due to the dissociation of surface silanol groups in aqueous medium. Instead, the PMMA particles are electrostatically stabilized through surface sulfate groups from the initiator during the polymerization process. The PMMA particles are constantly charged because the strongly acidic sulfate groups are fully dissociated in all relevant solution conditions.

To change the electrostatic double layer interactions (referred to as electrostatic interactions in the text), we varied the particle electric charge through the medium $p\text{H}$ [16]. Particle suspensions were diluted in buffer solutions of low ionic strength ($\leq 15\ \text{mM}$) by dialysis. A sample of 10 ml of particle suspension was dialyzed against 1 l of buffer solution for 5 h and next, the buffer solution was exchanged twice. We used a dialysis tubing cellulose membrane (D9652, Sigma Aldrich) with a size pore in the range of 1–2 nm. We assumed that the thermal Marangoni flow was negligible at room temperature in our aqueous systems. From surface tension measurements (see fig. S1 in Supplementary data), we also discarded other sources of Marangoni stress such as surfactant concentration gradients.

We measured the particle electrophoretic mobility as function of $p\text{H}$ value using a Zetasizer Nano device (Malvern, 4 mW He-Ne laser, 633 nm wavelength). The particle concentration used in the electrophoretic mobility measurements was $\Phi_m = 0.01\%$. The results are shown in fig. 2. The three different nanoparticles were negatively charged for the $p\text{H}$ values studied. The electric charge of the glass and SiO_2 nanoparticles at $p\text{H}$ 2 was very low and weak for the PMMA nanoparticles. Instead, all particles presented a maximum charge at $p\text{H}$ 9.

In drop evaporation, it is difficult to distinguish between diffusive and convective displacements of particles by imaging techniques. Besides, the Stokes-Einstein equation is not valid [22]. Due to this, we characterized the “free” diffusion of the nanoparticles in suspension, not confined. We measured the diffusion coefficient of the particles used in the driven menisci experiments with a

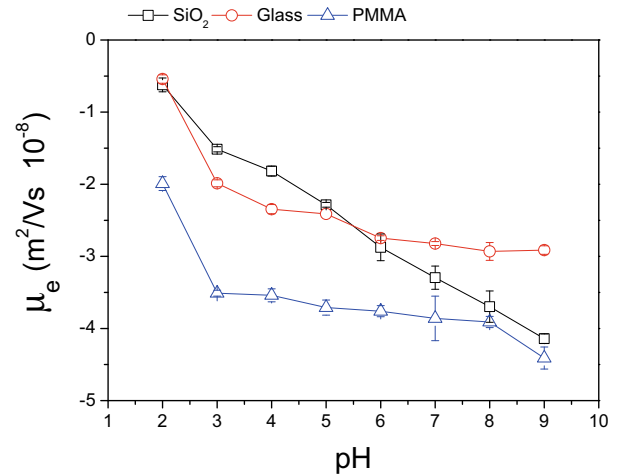


Fig. 2. Electrophoretic mobility as a function of $p\text{H}$ of the SiO_2 , glass and PMMA nanoparticles. The electrophoretic mobility measurements were performed at $\Phi_m = 0.01\%$.

particle size analyzer (ALV-GmbH, 3 mW He-Ne laser, 632.8 nm wavelength) operating in back scattering mode (detector at an angle of 173° with respect to the laser) to suppress multiple scattering contributions in concentrated systems [29]. The measurements were performed over the range of particle concentrations $\Phi_m = 0.1\text{--}20\%$ and for the weakest and strongest interparticle electrostatic repulsions ($p\text{H}$ 2 and $p\text{H}$ 9, respectively). The nanoparticle dispersions remained colloidally stable throughout the concentration range explored.

2.3 Driven menisci set-up

To produce the nanoparticle deposition in conditions similar to the standard dip coating technique, we controlled the receding motion of a meniscus confined between two vertical parallel plates. The sustained evaporation plays a very important role in the drying of nanoparticle suspensions at driven receding contact lines. However, evaporation and contact line dynamics can be decoupled at macroscopic scale [30,17,31,28]. Using this planar configuration, stripe-like deposits are typically obtained like the concentric rings found occasionally with evaporating sessile drops [32,33]. The “stick-slip” motion of the driven or free contact line is the responsible for this periodical deposit morphology although it depends on several parameters such as contact line velocity [34], temperature [35] or substrate wettability properties [28]. Our experimental device is shown in fig. 3. The substrates were placed in a glass cuvette (Hellma) with dimensions $50 \times 50 \times 10\ \text{mm}^3$. The cuvette was closed, not sealed. The substrates were carefully separated at the upper and lower positions to maintain a distance of 1 mm. The cuvette was filled with 15 ml of nanoparticle suspension and the meniscus was formed between the two parallel substrates by free capillary rise, which corresponded to the advancing meniscus configuration. In our set-up, the receding motion of the evaporating meniscus was driven by pumping out the sus-

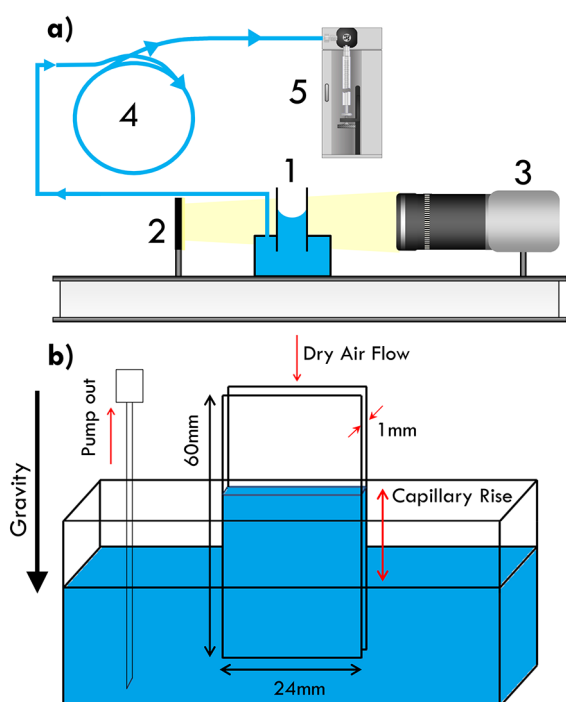


Fig. 3. (a) Layout of the set-up used for driven menisci experiments: 1) vertical cuvette, 2) planar light source, 3) B/W CCD camera, 4) collector tube of the outgoing suspension, filled with water and connected to the 5) microinjector. (b) Dimensions of the cell with the input of dry air and the pump-out system.

pension (reservoir) with a syringe (Hamilton, 12.5 ml) at constant flow rate ($3.47 \mu\text{l/s}$) using a microinjector (PSD3, Hamilton). To reach the receding configuration of the contact line from the beginning of each experiment, we manually removed a small amount of liquid from the reservoir with a syringe.

To monitor the contact line dynamics of the driven receding meniscus, we acquired images with a CCD (Retiga 1300, QImaging, $16 \mu\text{m}/\text{pixel}$) and backlight illumination at 1.7 fps during the entire experiment (approx. 1 hour). The images were analyzed using the software Mathematica. This way, the contact line position was determined as a function of time and the contact line velocity was estimated. During the entire experiment, the meniscus contact line and the reservoir level moved at the same velocity separated by a fixed distance (receding capillary rise). However, we examined the central region of the substrates, far from the borders, which corresponded to a maximum displacement of contact line of 14 mm (glass substrate). As a result, upon minimum evaporation (closed cuvette, $\text{RH} = 94\text{--}98\%$), we reproduced uniformly moving contact lines at $7 \mu\text{m/s}$, which agreed with the nominal linear velocity ($6.9 \mu\text{m/s}$).

The relative humidity was measured in situ with a humidity and temperature microsensors (Sensirion SHT71) under experimental conditions. We injected into the cuvette a flow of dry air ($\text{RH} = 2\%$), previously passed through drierite (Sigma-Aldrich), to reduce the actual RH

up to $\approx 65\%$. All experiments were carried out at room temperature ($20\text{--}23^\circ\text{C}$). From two experiments conducted with Milli-Q water at $\text{RH} = 65\%$ and 94% (without dry air) with glass substrates, we estimated the contact line velocity due to evaporation in roughly $1 \mu\text{m/s}$ (see fig. S2 in Supplementary data). In a strict sense, contact line dynamics in our experiments is ruled by the interplay of the local evaporation, at microscopic scale, and the driven motion. However, the overall evaporation and the dynamics of the whole liquid-vapor interface are de facto decoupled.

The final deposits were analyzed using the white light confocal microscope (PL μ , Sensofar Tech S.L.) with $50\times$ and $20\times$ objectives (Nikon, $285.8 \times 209.6 \mu\text{m}^2$ and $694.4 \times 510.09 \mu\text{m}^2$) and occasionally with a $10\times$ objective (Nikon, $1.39 \times 1.02 \text{mm}^2$). To visualize the deposits at lower scale, we utilized an atomic force microscope (Multi-Mode Scanning Probe Microscope Nanoscope IV, Veeco). To obtain a rough estimate of the amount of mass deposited (number of particles) in each case, we measured the area of the corresponding longitudinal profiles over a fixed substrate region and taking as zero level in height the bare surface of the substrate (found by scratching). Next, we computed the effective volume of the deposit by multiplying the former area by the substrate width (24 mm), because the patterns usually covered entirely the substrate surface. This effective volume was divided by the volume of a single particle. Although the particle packing in the deposits might depend on the deposition rate at the contact line, to reach an order of magnitude of the amount of material deposited, we indistinctly assumed that there were no gaps between the particles deposited.

3 Results and discussion

3.1 Diffusion coefficient of the nanoparticles

The results of light back-scattering experiments with the glass and PMMA nanoparticles at $\text{pH} 2$ and $\text{pH} 9$ are shown in fig. 4. When the interparticle electrostatic repulsion was strong (at $\text{pH} 9$, see fig. 2), we found that the diffusion coefficient increased as the particle concentration. However when the interparticle electrostatic interactions were weak (at $\text{pH} 2$, see fig. 2), a smaller increase of diffusion coefficient was observed compared with the observed at $\text{pH} 9$. It is known that, in photon correlation spectroscopy experiments [10], when the inverse of the scattering vector is much greater than the mean interparticle spacing (concentration dependent) then the measured intensity and its autocorrelation function are dominated by the collective diffusion of the particles. Due to this, for the size of particles studied, the range of concentration explored and the scattering angle and wavelength of our set-up, a crossover from self-diffusion to collective diffusion is actually measured. However, as expected, our results confirm that collective diffusion increases as particle concentration when the interparticle electrostatic repulsion is enhanced [10]. This effect should be more remarkable during the arrangement of charged particles at the triple line in the driven receding meniscus experiments.

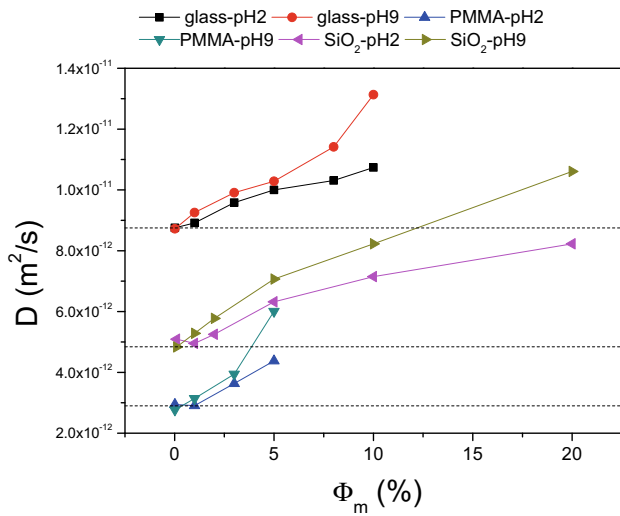


Fig. 4. Diffusion coefficient as a function of the concentration of glass, PMMA and SiO₂ nanoparticles at two pH values. Dashed lines represent the nominal (self-)diffusion coefficient calculated from the Stokes-Einstein relation for each nanoparticle.

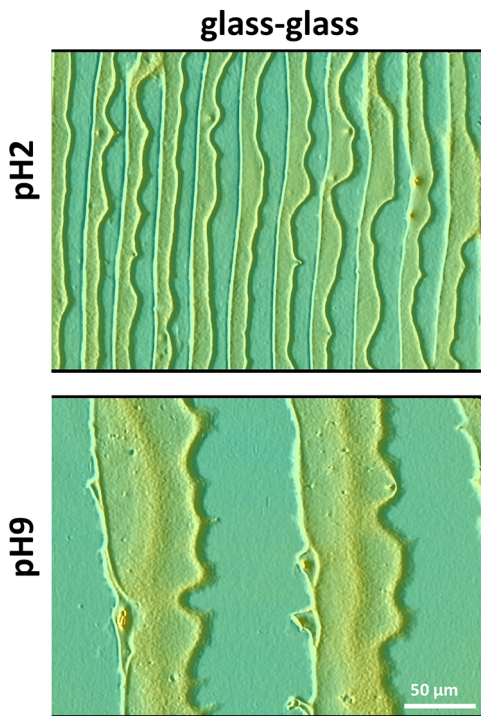


Fig. 5. Stripe-like deposits of glass nanoparticles at pH 2 and pH 9 on glass substrates obtained with the driven menisci set-up. The concentration of nanoparticles was $\Phi_m = 3\%$.

3.2 Driven menisci experiments: Effect of the particle-particle repulsion

The topographies of the stripe-like deposits formed on the glass substrates with weakly and strongly repulsive glass nanoparticles at $\Phi_m = 3\%$ are shown in fig. 5. Differences in the pattern morphology were observed when

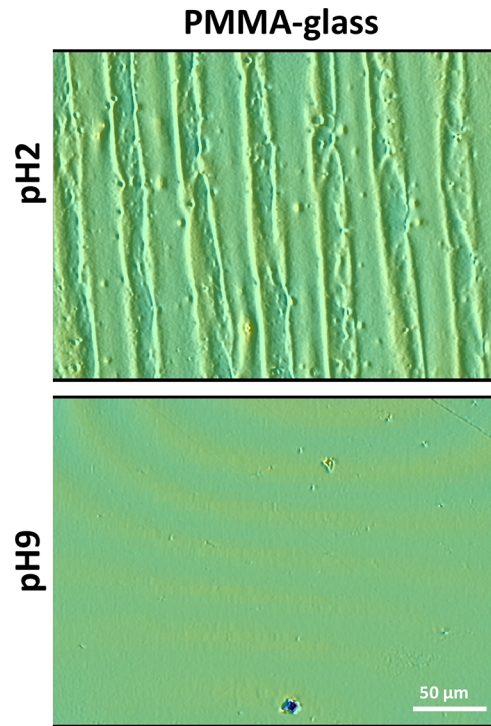


Fig. 6. Deposits of glass nanoparticles at pH 2 and pH 9 on PMMA substrates obtained with driven menisci experiments. The concentration of nanoparticles was $\Phi_m = 3\%$.

the particle-particle electrostatic interaction was varied. When the interparticle electrostatic repulsion was negligible (pH 2), the stripe width was smaller than the width in the pattern obtained with strong interparticle electrostatic repulsion (pH 9). When the substrate receding contact angle was changed, by using PMMA substrates, the results of deposition of glass nanoparticles at pH 2 and pH 9 were noticeably different (see fig. 6). The PMMA-glass system (substrate-particle system) at pH 2 revealed unresolved striped deposits although no particle deposit was formed at pH 9. To study the plausible role of the particle wettability in the deposit morphology, we performed driven menisci experiments with the glass-PMMA and PMMA-PMMA systems at pH 2 and pH 9. We also found different morphologies of striped patterns with the glass-PMMA system when the pH was changed. The greatest deposits (width and height) were obtained with the PMMA-PMMA system at pH 2 but no particle deposition was observed at pH 9, as happened with the PMMA-glass system.

We classified the different substrate-particle systems studied into symmetrical and asymmetrical systems. In fig. 7, we plot the deposit profiles for each type of system. The striped patterns formed with the glass-glass system and the large stripe obtained with the PMMA-PMMA system at pH 2 are confirmed. The distance between stripes formed with the PMMA-PMMA system at pH 2 was so large that only one stripe at once could be visualized with the 10× objective. No deposition was found with the PMMA-PMMA system at pH 9. At pH 2, stripe-like

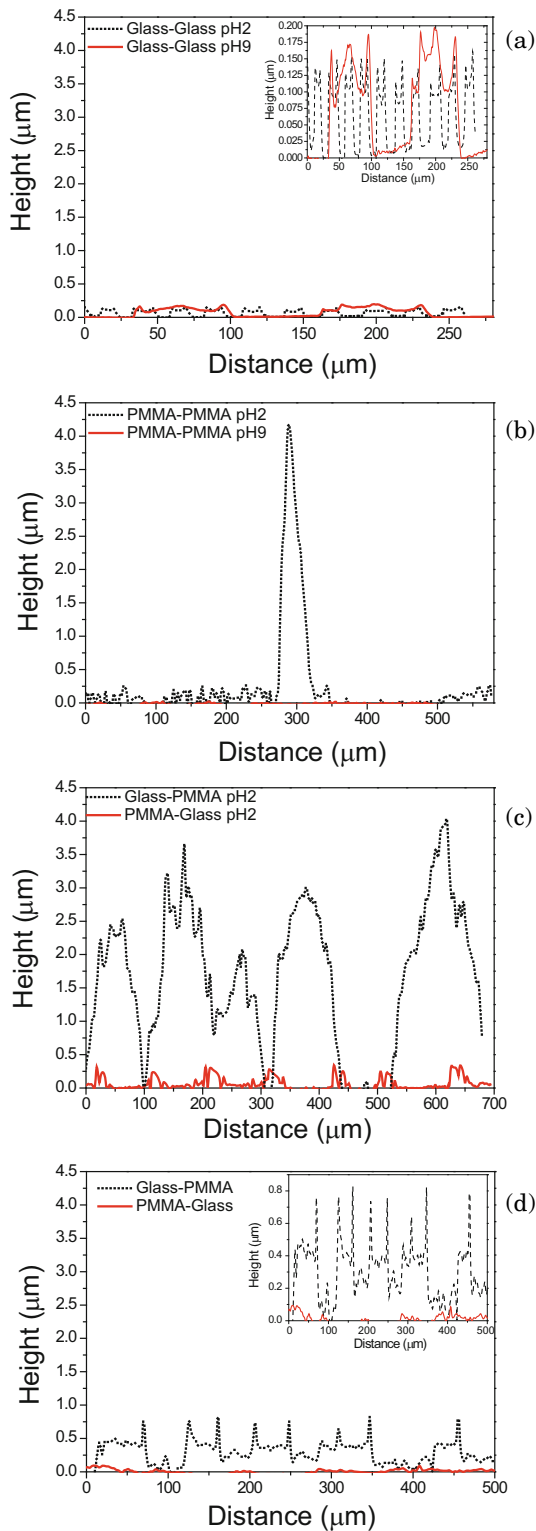


Fig. 7. Deposit profiles formed with the symmetrical substrate-particle systems at pH 2 and pH 9: (a) Glass-glass system and (b) PMMA-PMMA system and the asymmetrical substrate-particle systems at (c) pH 2 and (d) pH 9. The concentration of nanoparticles was $\Phi_m = 3\%$.

deposits were also obtained with the asymmetrical systems. Although the distance between stripes was very similar in both systems, the glass-PMMA system revealed

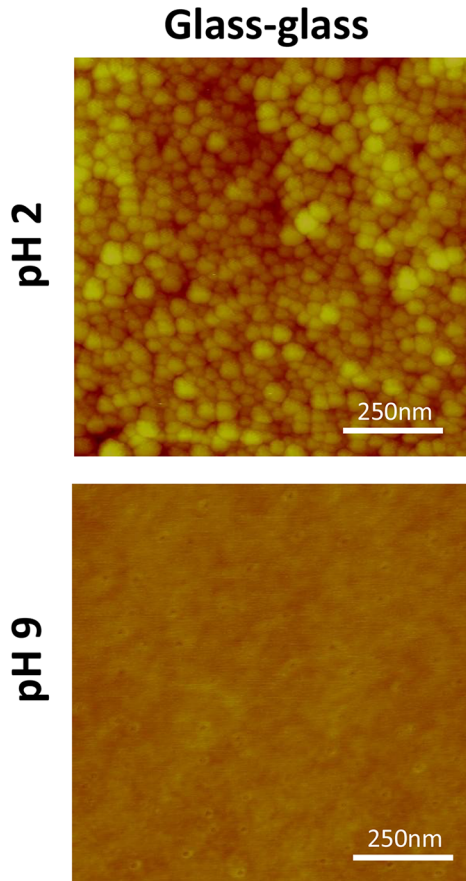
much higher deposits but it cannot be explained by the larger size of the PMMA nanoparticles. Instead, at pH 9, a striped pattern was obtained with the glass-PMMA system but no deposit was formed with the PMMA-glass system. These results are summarized in table 1.

The main feature of the symmetrical systems is that the substrate-particle wettability contrast (differences between receding contact angles) is minimized. Otherwise, in the asymmetrical systems, the wettability contrast is negative for the glass-PMMA system and positive for the PMMA-glass system. However, there is no correlation between the substrate-particle wettability contrast and the final deposit (see table 1). When the substrate used was PMMA at pH 9, no deposit was formed regardless of the type of nanoparticle used. The glass and PMMA nanoparticles at pH 9 may develop higher collective diffusion if a concentration gradient in the suspension is established. Further, these nanoparticles are subjected to a moderate convective flow due to the high receding contact angle of the substrate. As consequence, the nanoparticle deposition at driven receding contact lines was unfavored because the significant diffusive flow canceled or overcame the outward convective flow. Unlike the case PMMA-glass at pH 2, when the PMMA nanoparticles were used in the same conditions (PMMA-PMMA at pH 2), the deposits were unexpectedly high and distant. Further work should be addressed to understand this result. To examine the effect of the diffusive flow when the convective flow is minimized, we performed menisci experiments with the glass-glass and PMMA-glass systems at pH 2 and pH 9. These experiments were carried out under vapor-saturated conditions, with no dry air flow in the closed cuvette. This way the relative humidity inside the cuvette increased up to $\approx 94\%$. The AFM images obtained for the glass-glass system are shown in fig. 8. Particle deposits were only found at pH 2. The residual convective flow on the (very hydrophilic) glass substrate was still significant compared with the collective diffusion of nanoparticles at pH 2. In the PMMA-glass system, where the convective flow was much less noticeable than on the glass substrate, no deposit was found at both pH values. Since the convective flow at $RH \approx 94\%$ was significantly reduced regardless of the substrate receding contact angle, the flow was completely suppressed by collective diffusion at pH 9.

The substrate charge at low ionic strength seems to be irrelevant in this scenario [15], where the intense flows developed close to the triple line are capable to drag charged particles even very close to the like-charged substrate. We have observed with fluorescence confocal microscopy [36] that positively and negatively charged particles are transported towards the contact line at a lower rate than nearly uncharged particles, regardless of the substrate used. Further, we have observed by optical microscopy (not shown) how charged particles on like-charged substrates are mostly trapped at receding contact lines rather than barely charged particles. This proves that the charged particles are not arrested by the surface and become laterally mobile. Instead, since the convective flow collects a greater number of barely charged particles close

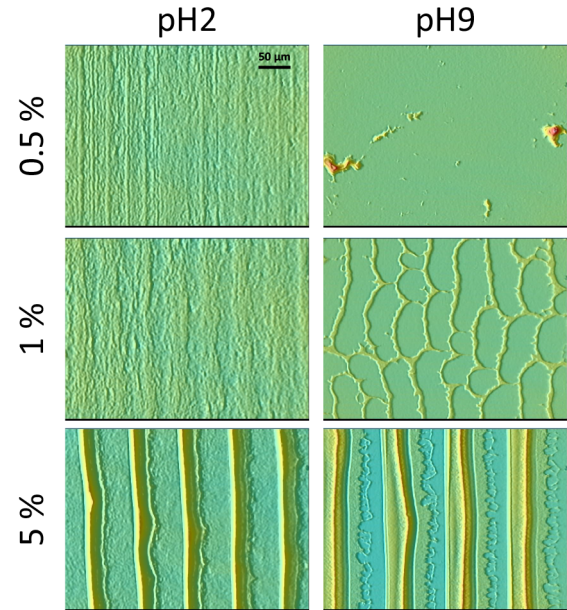
Table 1. Deposit formed with the symmetrical and asymmetrical systems.

Nanoparticle	Glass substrate	PMMA substrate
Barely charged glass (<i>pH</i> 2)	Stripe-like deposit	Weak stripe-like deposit
Charged glass (<i>pH</i> 9)	Stripe-like deposit	No deposit
Barely charged PMMA (<i>pH</i> 2)	Uneven stripe-like deposit	Unresolved stripe-like deposit
Charged PMMA (<i>pH</i> 9)	Stripe-like deposit	No deposit

**Fig. 8.** Atomic force microscopy images of the deposits obtained with driven menisci experiments under saturation conditions ($RH \approx 94\%$) for the glass-glass system at *pH* 2 and *pH* 9.

to the triple line, self-pinning is enhanced. The role of the substrate seems to be more relevant through its receding contact angle by a two-fold effect: the size of wedge-shaped region near the contact line and the magnitude of the evaporation-driven convective flow.

Regarding the (primary) electroviscous effect [37] on the collective diffusion coefficient of stabilized colloidal suspensions, we are aware of the plausible impact of the particle charge on the water viscosity in the vicinity of the particle surface. The expected increase of the viscosity of a suspension containing interacting particles beyond the dilute limit [37] should indeed reveal their collective diffusive motion (see fig. S3 in Supplementary data). To in-

**Fig. 9.** Deposits of SiO_2 nanoparticles at *pH* 2 and *pH* 9 on glass substrates with driven menisci experiments. The concentration of nanoparticles was $\Phi_m = 0.5, 1$ and 5% .

clude the electroviscous effect in the calculation of the collective diffusion coefficient of interacting particles is certainly difficult. It is known that the electrolyte friction of a single spherical nanoparticle has a weak effect on the self-diffusion coefficient [38]. The results obtained in this work with the strongly charged PMMA particles on two different substrates (PMMA and glass) and on the same substrate (glass) but at two different *RH* values (65% and 94–98%) point out that the primary electroviscous effect was negligible.

3.3 Driven menisci experiments: Effect of the nanoparticle concentration

To examine the effect produced by the nanoparticle concentration on the patterning, we conducted experiments on glass substrates with the SiO_2 nanoparticles at increasing concentrations ($\Phi_m = 0.5\text{--}30\%$), and at two *pH* values (*pH* 2 and *pH* 9). This way, the convective flow was fixed by the substrate receding contact angle.

It is clear the transition found in the pattern morphology as the particle concentration was changed, although with differences as the *pH* value used (see fig. 9).

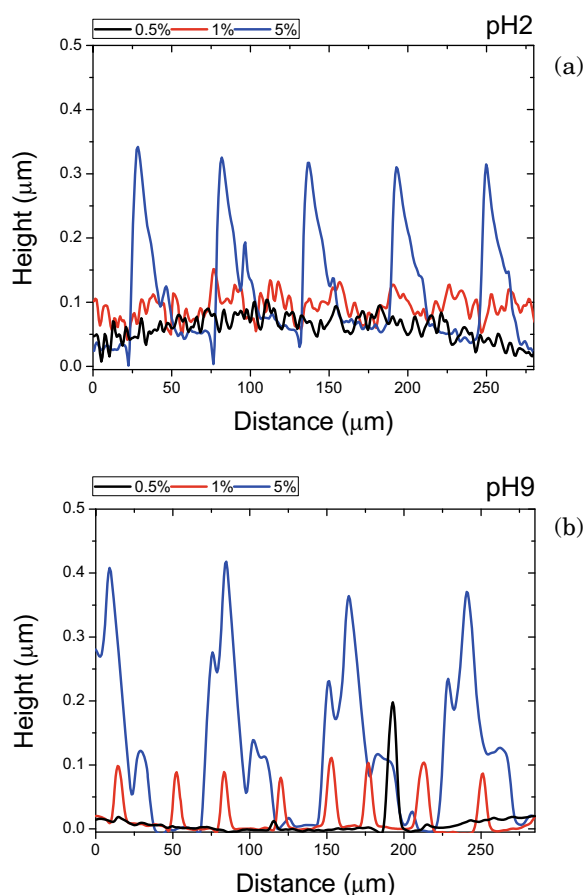


Fig. 10. Deposit profiles formed with the glass-SiO₂ system at (a) pH 2 and (b) pH 9. The concentration of nanoparticles was $\Phi_m = 0.5, 1$ and 5%.

The deposit profiles are shown in fig. 10. The nearly uncharged nanoparticles formed patterns even at 0.5%, although unresolved. With these particles, the substrate was completely covered (see fig. 10(a)). Otherwise, when the nanoparticles were charged, almost no deposit was found at 0.5% although a spiderweb-like deposit was found at 1%. However, well-defined striped patterns were formed with both particles at 5%. At higher concentrations (topographies not shown), the resulting striped patterns were more complex due to the plausible occurrence of Marangoni recirculating flows (see fig. S1-b in Supplementary data) and the increase of viscosity (see fig. S3 in Supplementary data). The difference found at low particle concentrations might be explained in terms of competition between the outward convective and inward diffusive flows. Compared to the barely charged particles, lower number of charged particles was transported towards the contact line because they preferred to diffuse towards the bulk (see fig. 4).

From the profiles of fig. 10, the amount of mass deposited was estimated. The number of SiO₂ nanoparticles deposited on glass substrates for increasing concentrations is plotted in fig. 11. Significant differences are observed as the particle electric charge. The amount of material

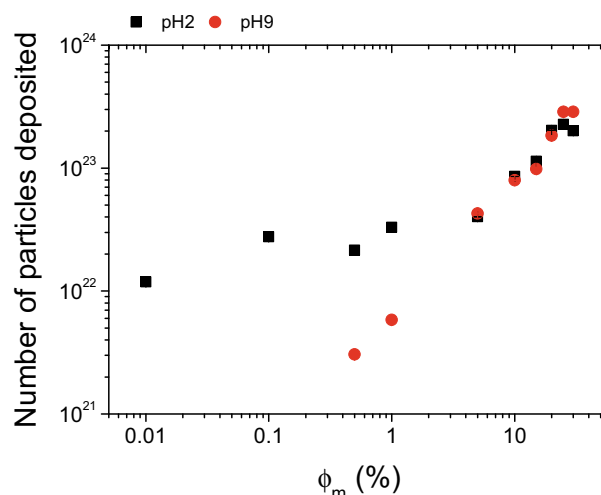


Fig. 11. Number of SiO₂ nanoparticles deposited on glass substrates with driven menisci experiments in terms of the particle concentration. The nanoparticles were nearly uncharged (pH 2) and charged (pH 9). For concentrations below 0.5%, the charged particles did not form deposits.

forming the deposits is noticeably greater with the barely charged nanoparticles (pH 2) up to $\Phi_m = 5\%$. From this concentration, the number of SiO₂ nanoparticles deposited was independent of the pH value. Instead, the deposits formed with the charged nanoparticles grew steadily as the particle concentration up to $\Phi_m = 25\%$, where the deposit growth seems to saturate. The plausible decrease of the concentration gradient between the triple line and the suspension as the bulk concentration increases might explain the disagreement found between the nearly uncharged and charged nanoparticles at low concentration. According to Fick's law, a lower gradient mitigates the collective diffusion even for the charged nanoparticles.

4 Conclusions

Unlike typical experiments of free drop evaporation, evaporating menisci experiments with driven receding contact lines allow to explore convective assembly at fixed and low bulk concentration, which enables to develop high concentration gradients. Particle deposition at driven receding contact lines may be controlled by the interplay between evaporative convection and collective diffusion. When the evaporation flow is weak, deposition can be suppressed if the long-range interparticle repulsion becomes important and the diffusion overcomes the particle transport by convection before reaching the triple line. In this scenario, the receding contact angle of the substrate and the relative humidity dictate the strength of the convective velocity field. Diffusive flow takes relevance at low particle concentration, when the gradient between the contact line and bulk is important. In this case, the particle-particle repulsion produces a significant transition in the final pattern morphology and reduces the number of particles deposited.

This work was supported by the “Ministerio Español de Economía y Competitividad” (project MAT2014-60615-R) and the “Junta de Andalucía” (project P12-FQM-1443). D. Noguera thanks the Biocolloid and Fluid Physics Group (ref. PAI-FQM115) of the University of Granada (Spain) and Dr. Juan de Vicente for help with the viscosity measurements. C. Moraila thanks the University of Sinaloa (Mexico).

References

- Z. Lin (Editor), *Evaporative Self-Assembly of Ordered Complex Structures* (World Scientific, Singapore, 2012).
- R.D. Deegan, O. Bakajin, T.F. Dupont, G. Huber, S.R. Nagel, T.A. Witten, *Nature* **389**, 827 (1997).
- H. Hu, R.G. Larson, *Langmuir* **21**, 3963 (2005).
- R.D. Deegan, O. Bakajin, T.F. Dupont, G. Huber, S.R. Nagel, T.A. Witten, *Phys. Rev. E* **62**, 756 (2000).
- E. Widjaja, M.T. Harris, *AIChE J.* **54**, 2250 (2008).
- F. Doumenc, B. Guerrier, *Langmuir* **26**, 13959 (2010).
- L. Frastia, A.J. Archer, U. Thiele, *Phys. Rev. Lett.* **106**, 077801 (2011).
- G. Nägele, *Phys. Rep.* **272**, 215 (1996).
- G.K. Batchelor, *J. Fluid Mech.* **74**, 1 (1976).
- D.N. Petsev, N.D. Denkov, *J. Colloid Interface Sci.* **149**, 329 (1992).
- P.N. Segrè, O.P. Behrend, P.N. Pusey, *Phys. Rev. E* **52**, 5070 (1995).
- S.S.L. Peppin, J.A.W. Elliott, M.G. Worster, *J. Fluid Mech.* **554**, 147 (2006).
- L. Daubersies, J.B. Salmon, *Phys. Rev. E* **84**, 031406 (2011).
- R. Bhardwaj, X. Fang, P. Somasundaran, D. Attinger, *Langmuir* **26**, 7833 (2010).
- S. Das, S. Chakraborty, S. Mitra, *Phys. Rev. E* **85**, 046311 (2012).
- C.L. Moraila-Martinez, M.A. Cabrerizo-Vilchez, M.A. Rodríguez-Valverde, *Soft Matter* **9**, 1664 (2013).
- C. Hsueh, C.L. Moraila-Martínez, F. Doumenc, M.A. Rodríguez-Valverde, B. Guerrier, *Chem. Eng. Proc.* **68**, 64 (2013).
- F. Carle, D. Brutin, *Langmuir* **29**, 9962 (2013).
- V.R. Dugyala, M.G. Basavaraj, *Langmuir* **30**, 8680 (2014).
- A. Sarkar, M.S. Tirumkudulu, *Langmuir* **25**, 4945 (2009).
- I. Nikiforow, J. Adams, A.M. König, A. Langhoff, K. Pohl, A. Turshatov, D. Johannsmann, *Langmuir* **26**, 13162 (2010).
- A. Merlin, J. Angly, L. Daubersies, C. Madeira, S. Schöder, J. Leng, J.B. Salmon, *Eur. Phys. J. E* **34**, 1 (2011).
- A. Askounis, K. Sefiane, V. Koutsos, M.E. Shanahan, *Colloids Surf., A* **441**, 855 (2014).
- D. Noguera-Marn, C.L. Moraila-Martnez, M.A. Cabrerizo-Vilchez, M.A. Rodríguez-Valverde, *Langmuir* **31**, 6632 (2015).
- F.J.M. Ruiz-Cabello, M.A. Rodríguez-Valverde, M.A. Cabrerizo-Vilchez, *J. Adhes. Sci. Technol.* **25**, 2039 (2011).
- C.L. Moraila-Martínez, F.J.M. Ruiz-Cabello, M.A. Cabrerizo-Vilchez, M.A. Rodríguez-Valverde, *Colloids Surf., A* **404**, 63 (2012).
- H. Radelczuk, L. Hoysz, E. Chibowski, *J. Adhes. Sci. Technol.* **16**, 1547 (2002).
- D. Noguera-Marín, C.L. Moraila-Martínez, M.A. Cabrerizo-Vilchez, M.A. Rodríguez-Valverde, *Langmuir* **30**, 7609 (2014).
- S. Ramakrishnan, S.A. Shah, L. Ruggeri, Y.L. Chen, K.S. Schweizer, C.F. Zukoski, *Langmuir* **25**, 10507 (2009).
- H. Bodiguel, F. Doumenc, B. Guerrier, *Langmuir* **26**, 10758 (2010).
- F. Doumenc, B. Guerrier, *EPL* **103**, 14001 (2013).
- E. Adachi, A.S. Dimitrov, K. Nagayama, *Langmuir* **11**, 1057 (1995).
- W. Sun, F. Yang, *J. Phys. Chem. C* **118**, 10177 (2014).
- U. Thiele, *Adv. Colloid Interface Sci.* **206**, 399 (2014).
- H. Uchiyama, D. Shimaoka, H. Kozuka, *Soft Matter* **8**, 11318 (2012).
- D. Noguera-Marín, C.L. Moraila-Martínez, M.A. Cabrerizo-Vilchez, M.A. Rodríguez-Valverde, *Soft Matter* **11**, 987 (2015).
- D.B. Genovese, *Adv. Colloid Interface Sci.* **171-172**, 1 (2012).
- A. Vizcarra-Rendón, M. Medina-Noyola, R. Klein, *Chem. Phys. Lett.* **173**, 397 (1990).